A Non-Destructive and Position-Unrestricted Integrated Photonic Chip Detection Method

Jinze Shi, Changying Li, Jiajun Wan, Xiaoping Liu

1 Abstract

As the number and diversity of devices integrated into photonics systems continue to grow, the complexity of system composition also escalates. It becomes increasingly challenging to pinpoint the exact location and condition of internal faults within an on-chip system relying solely on couplers positioned at specific preprocessed locations. Coherent pump beams' interference has the capability to induce a periodic carrier distribution in the material, thus modulating the refractive index and effectively creating a diffraction grating. In this study, a non-destructive and position-agnostic detection method based on a carrier grating is proposed. We develop a comprehensive theoretical model to calculate carrier dynamics under various pump configurations. Leveraging the Finite-Difference Time-Domain (FDTD) method and accounting for Free Carrier Index (FCI) and Free Carrier Absorption (FCA) effects, meticulous analysis of the quantitative impact of pump intensity and radius on the diffraction efficiency of the carrier grating and its far-field divergence characteristics are provided. Ultimately, this research contributes to a discussion on the feasibility of high spatial resolution experimental approaches.

2 Introduction

The compatibility of integrated photonics with COMOS processes has led to rapid advancements in the field, offering significant potential applications in areas such as sensing, computation, and communication[1]. However, as on-chip device scale and system complexity continue to grow, drawbacks such as processing deviations and long fabrication cycles not only burden the design and iteration of on-chip systems[2] but also increase the difficulty of detecting actual system defects. Traditional on-chip system detection methods rely on input and output information. For instance, in photonics computing systems, the system's normal operation can be inferred from the output signal given a specific input. In this context, the system can be likened to a black box within a circuit, and the complexity of the system makes it challenging to determine the mode propagation characteristics at a specific location based solely on output information. The primary objective of this work is to present a "voltmeter for optics," a non-destructive method for measuring the optical field at any arbitrary position within a photonic chip system.

The input and output of integrated photonics chips typically require connections to free space or optical fibers, with coupler being the most commonly used means. Depending on their location, coupler can be categorized as edge coupler and grating coupler[3]. In cases where high bandwidth requirements are not necessary, grating coupler are often more suitable due to their flexible fabrication positions that need not be limited to the chip's edges. Grating couples are based on the principle of altering wave vector through grating, where specific fabrication period can achieve coupling in or out along specific direction[4]. In its essence, grating involve materials with periodic variations in refractive index. This periodic variation can be achieved not only through alternating materials but also through periodic distribution of physical field within the same material, such as temperature, stress, carrier concentration, etc. Therefore, in line with the concept of grating coupler, generating a grating by introducing a periodic variation of a physical field at a specific location on the chip is a way to achieve detection at arbitrary on-chip positions. This technique is generally referred to as Transient Grating Spectroscopy (TGS)[5]. TGS employs two coherent pulsed

pump beams to generate interference pattern on the sample surface, as shown in Figure 1 (a). This interference pattern results in a periodic distribution of physical field. By adjusting the delay τ of the probing light (Figure 1 (b)), dynamic processes like carrier transport can be characterized. Spatially periodic optical field can induce a spatially periodic carrier concentration, and according to the plasma effect[6], the material's dielectric coefficient also periodically changes in space, leading to the grating effect known as a carrier grating.

For bulk materials, research utilized pump light with wavelengths greater than the silicon bandgap (1.1 eV) to create a carrier grating in bulk silicon material and used this grating to measure carrier lifetimes[7]. In the SOI (Silicon-on-Insulator) system, research has explored the off-chip reconfigurable analysis of integrated devices using pump light and a Spatial Light Modulator (SLM) [8−10]. Additionally, studies have employed pump-probe techniques to measure dynamic processes such as single-photon absorption(SPA)[11], two-photon absorption(TPA)[12], Auger recombination[13], and surface recombination[14] in waveguides. However, there is currently no research on characterizing integrated photonics systems or device performance using TGS technology. The carrier grating's efficiency in coupling out propagation modes or, in other words, its diffraction efficiency (the ratio of diffracted intensity to incident intensity[15]) for waveguides is a critical quantitative analysis. This paper will quantitatively discuss the diffraction efficiency of carrier grating in SOI systems and the feasibility of experiments in the following sections. Section 3 primarily discusses the preconditions involved in carrier grating, including wave vector analysis, plasma effect and damage threshold. Section 4 conducts theoretical analysis on carrier dynamics. Section 5 utilizes FDTD method to stimulate diffraction efficiency and far-field divergence under different refractive index maps. Section 6 presents an analysis and discussion of experimental configurations, and finally, the conclusion is provided in the last section.

3 Preconditions

3.1 Wave Vector Analysis

As shown in Figure. 1(a), two coherent pump beams generate interference fringes on the sample surface with a fixed period Λ. The relationship between the fringe period and the angle ψ of the pump beams is given by:

$$|\vec{k_1}|sin(\phi) + |\vec{k_2}|sin(\phi) = 2\pi/\Lambda$$
$$|\vec{k_1}| = |\vec{k_2}| = \frac{2\pi n_{cladding}}{\lambda_{pump}}$$

(1)

For a fixed wavevector of the probe light, changing the grating's period can alter the direction of its diffraction signal. A similar analysis can be applied to the SOI architecture, taking a strip waveguide as an example, as illustrated in Figure. 1(c). The probe light represents a propagating mode within the waveguide. The wavevector of the first-order diffracted light must satisfy the phase-matching condition, as depicted in Figure. 1(d), which can be expressed as:

$$|\vec{k_3}| - K = |\vec{k_4}|sin(\theta)$$
$$|\vec{k_3}| = 2\pi n_{eff}/\lambda_{probe}$$
$$|\vec{k_4}| = 2\pi n_{cladding}/\lambda_{probe}$$

(2)

Here, n_{eff} represents the effective refractive index of the propagating mode within the waveguide, and $n_{cladding}$ is the refractive index of the waveguide's cladding. To ensure the presence of diffracted light, the grating period must satisfy $K < 2|\vec{k_3}|$. Otherwise, the grating period would fall into the range of Subwavelength Grating (SWG)

structures and would not serve as a diffraction grating. To avoid multiple diffraction orders and energy losses caused by oblique incidence at the cladding-air interface, making the diffraction signal emerge perpendicularly, i.e., $\theta = 0$, is a suitable choice.
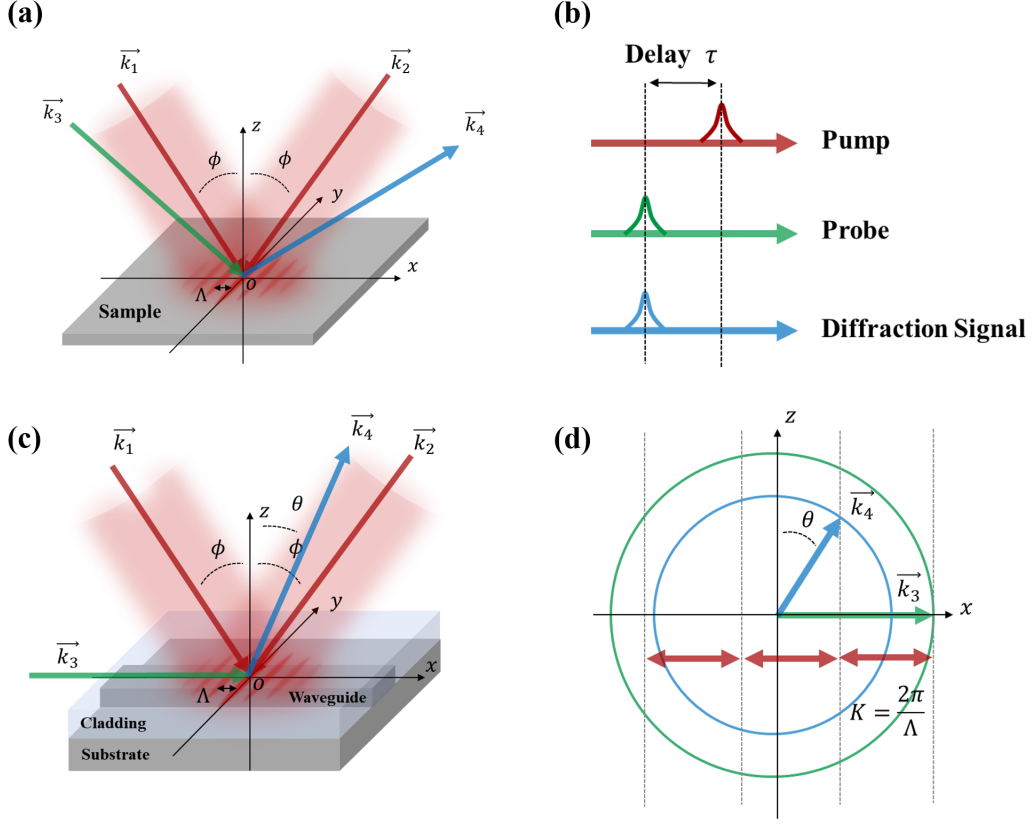

Figure. 1 (**a**)Schematic diagram illustrating the wavevector relationships in TGS. $\vec{k_1}$, $\vec{k_2}$, $\vec{k_3}$, and $\vec{k_4}$ represent the wavevectors of the two pump beams, the probe light, and the diffracted signal, respectively. (**b**)Diagram depicting the time-delay relationships between the pump beams, probe light, and diffracted light. (**c**)Schematic illustration of the wavevector relationships in the TGS setup for the SOI system. (**d**)Phase-matching relationships for different types of wavevectors.

3.2   Plasma Effect

The plasma effect, also known as the plasma dispersion effect or plasma resonance effect, is a phenomenon where free carriers in a material interact with electromagnetic waves, resulting in changes in the material's real part of refractive index (Free Carrier Index or FCI) and imaginary part of refractive index (Free Carrier Absorption or FCA). Theoretically, quantitative relationships can be derived through various models[16] to describe these effects. However, in practical applications, empirical formulas based on experimental observations are often used to describe the relationships between FCI, FCA, and carrier concentrations[17].

$$\widetilde{n} = n + ik$$

$$\Delta n = -[8.8 \times 10^{-4} N_e + 8.5(N_h)^{0.8}] \times 10^{-18} \tag{3}$$

$$\Delta k = \frac{\lambda}{4\pi}[8.5 N_e + 6.0 N_h] \times 10^{-18}$$

N_e and N_h represent the concentrations of electrons and holes, respectively, and their units are cm^{-3}. Figure.

3

2 depicts the relationship between the absolute values of the real and imaginary parts of the refractive index and the concentrations of both types of carriers. Concerning the real part of the refractive index, in the region where the concentration is less than $10^{18}cm^{-3}$, the influence of electron concentration is more significant than that of hole concentration. In the high-concentration region, both types of carriers have a similar impact on the real and imaginary parts of the refractive index. It's only when the concentration approaches $10^{20}cm^{-3}$ that there is 0.1 magnitude change in the refractive index, indicating that to enhance the coupling efficiency of the grating, it is necessary to increase the intensity of the pump light intensity($W \cdot \mu m^{-2}$) to generate more carriers per unit time. However, this introduces a new issue: will increasing the laser intensity potentially damage (e.g., burn holes or melt) the on-chip system and devices?
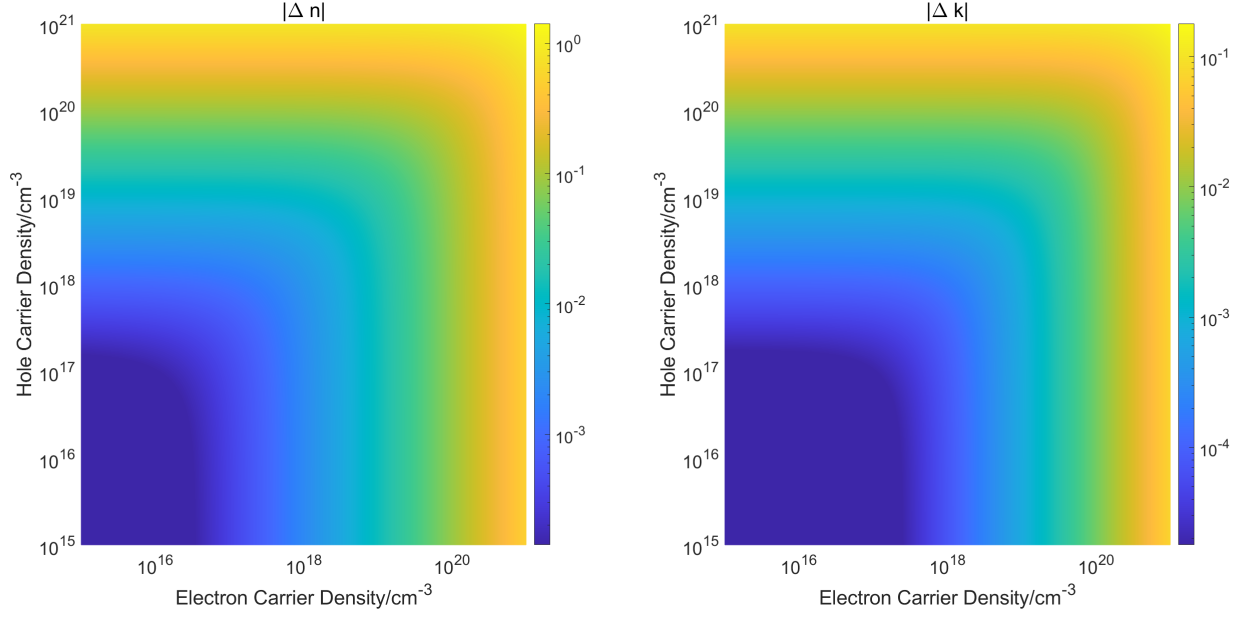

Figure. 2 Change in absolute values of refractive index real and image parts induced by free Electrons and Holes concentration.

3.3 Damage Threshold

The damage threshold is defined as the upper limit of laser intensity to prevent the chip from being damaged. Its physical meaning is the laser power per area. For pulsed pump light, whose power varies with time and space, the damage threshold corresponds to the peak light intensity of each pump pulse. When the laser energy density is too high, it can lead to a situation where the rate of carrier generation exceeds the relaxation rate, resulting in heat accumulation that raises the temperature of the chip material. If the temperature exceeds the melting point, the chip can be damaged. For different pulse durations, different physical processes involving relaxation come into play, and the order of magnitude of the damage threshold varies accordingly. For example, with a pulse duration of 10 ps(i.e.,intensity reduces to $1/e^2$ at 5ps from the peak time), the main processes involved are carrier generation and recombination. At the 10 ns level, carrier diffusion also plays a role, and at 10 ms or continuous light levels, thermal diffusion becomes significant. Reducing the pulse duration significantly increases the order of magnitude of the damage threshold. For silicon material pumped by a laser wavelength of 1064 nm as an example, the damage threshold for a 10 ps pulse is $823.93W \cdot \mu m^{-2}$, and for a 10 ns pulse, it is $5.64W \cdot \mu m^{-2[18]}$. From picosecond to nanosecond pulased laser, decreasing the time scale by three orders of magnitude results in a increase of two orders of magnitude in the damage threshold. Although smaller time scales lead to higher damage thresholds, they also

require stricter experimental time precision. To provide a more comprehensive analysis of experimental feasibility, this discussion will also consider cases with relatively larger pulse durations. To ensure that the chip is not damaged, the modeling discussed below will set the pulse pump light intensity to be lower than the damage threshold.

4 Carrier Dynamics Analysis

4.1 interference Generation

As shown in the illustration of Figure. 1(c), within the coherent optical path range, the pump light field can be expressed as follows form of plane wave:

$$\begin{aligned}
\widetilde{E_1} &= |\widetilde{E_1}|e^{-i(\vec{k_1}\cdot\vec{r}-\omega t)} \\
\widetilde{E_2} &= |\widetilde{E_2}|e^{-i(\vec{k_2}\cdot\vec{r}-\omega t)}
\end{aligned} \tag{4}$$

where $\vec{r}$ is the point concerned, and ω represents frequency of the light. At the sample surface, i.e., at $z = 0$, the optical fields superpose. For simplification, let's consider the intensity distribution $I(x)$ along the waveguide's extension direction (x-direction). This can be derived as follows:

$$I(x) = |\widetilde{E_1} + \widetilde{E_2}|^2 = |\widetilde{E_1}|^2 + |\widetilde{E_2}|^2 + 2|\widetilde{E_1}||\widetilde{E_2}|cos(\frac{2\pi}{\Lambda}x) \tag{5}$$

Considering that the detection method needs to have a certain spatial resolution. In practical experiments, the pump light field cannot be assumed to be a plane wave but rather exhibits a Gaussian form with a certain spatial width:

$$\begin{aligned}
|\widetilde{E_1}|^2(x, z=0) &= I_1 e^{[-x^2 cos(\phi)^2/a_1^2]} \\
|\widetilde{E_2}|^2(x, z=0) &= I_2 e^{[-x^2 cos(\phi)^2/a_2^2]}
\end{aligned} \tag{6}$$

where a_1 and a_2 are the Gaussian radius (the length where intensity reaches $1/e^2$ of the peak's value) of the pump beams, I_1 and I_2 are the central intensities of the pump light field. Assuming that the two beams are from the same source and are split, their intensities and radii are consistent, i.e., $a_1 = a_2 = a$, $I_1 = I_2 = I_0$. Considering the interface reflectivity R, the interference optical intensity information can be written as:

$$I(x) = 2I_0(1-R)e^{[-x^2 cos(\phi)^2/a^2]}[1 + cos(\frac{2\pi}{\Lambda}x)] \tag{7}$$

The interference fringe period Λ is set to ensure that the diffracted light exits the waveguide surface perpendicularly, i.e., $K = |\vec{k_4}| \to \Lambda = \lambda/n_{eff}$. Since the interference fringe period is fixed, changes in the detection spatial resolution - the radius $r_0 = a/cos(\phi)$ of the carrier grating - will influence the number of fringes at a detection point. The number of fringes not only affects the diffraction efficiency of the grating but also influences the divergence characteristics of the diffracted light. Concerning diffraction, only the intensity distribution with periodic variations affects the coupling, while the non-periodic part only introduces undirected scattering[20]. Therefore, it is necessary to define a variable which could represent the periodic portion of the pump $I(x)$, which can be treated as a Gaussian-shaped DC signal supposed with another Gaussian-shaped AC signal. The range of this AC part, defined as Δ which equals to $4I_0(1-R)$ in equation (7), accounts a significant matter in grating. The above intensity distribution only deals with spatial distribution and does not account for temporal changes. In reality, the pump light intensity also entirely varies over time. Therefore, studying the evolution of the range Δ of the periodic parts

of carriers concentration over time is crucial for analyzing the diffraction efficiency of the carrier grating. This will be discussed in detail in the following parts.

4.2 Carrier Dynamics

The generation and recombination of carriers involve various nonlinear physical processes, and dynamic modeling is required for electrons and holes separately. Silicon material has a bandgap of 1.12 eV, which means that light with wavelengths shorter than 1070 nm can excite valence band electrons into the conduction band, thereby generating free carriers (electrons and holes). The two primary mechanisms for the generation of free carriers under the influence of the pump light are single photon absorption (SPA), where one photon is absorbed in the transition, and two-photon absorption (TPA), where two photons are simultaneously absorbed. Higher-order nonlinear processes require higher optical intensities for pumping. In bulk materials, the recombination of free carriers from the conduction band to the valence band mainly occurs through Auger recombination and radiative recombination. Auger recombination becomes significant typically at carrier concentrations on the order of $10^{19} cm^{-3}$ or higher, which is necessary for the configuration studied in this paper. Defective semiconductors introduce energy states between the conduction and valence bands, leading to Shockley-Read-Hall (SRH) recombination. Defect states near the material's surface can also lead to surface recombination. However, the effective range of surface recombination for silicon and silicon dioxide is approximately 50 nm from the surface[21]. In the discussion below, we will focus on a 1 μm wide waveguide as the research subject and temporarily neglect SRH recombination and surface recombination. Therefore, the evolution of electron and hole concentrations over time can be described as follows:

$$\frac{\partial N(x,t)}{\partial t} = \alpha(1-R)I(x,t)/h\nu + \beta(1-R)I(x,t)^2/2h\nu - C_n[N(x,t)^2 P(x,t) - n_0^2 p_0]$$
$$- C_p[N(x,t)P(x,t)^2 - n_0 p_0^2] - B[N(x,t)P(x,t) - n_0 p_0] \tag{8}$$

$$\frac{\partial P(x,t)}{\partial t} = \alpha(1-R)I(x,t)/h\nu + \beta(1-R)I(x,t)^2/2h\nu - C_n[N(x,t)^2 P(x,t) - n_0^2 p_0]$$
$$- C_p[N(x,t)P(x,t)^2 - n_0 p_0^2] - B[N(x,t)P(x,t) - n_0 p_0] \tag{9}$$

$$I(x,t) = I(x)e^{-(t-t_0)^2/\tau^2} \tag{10}$$

In the above equation, α and β represent the SPA and TPA coefficients, respectively. $h\nu$ is the energy of a single photon, C_n, C_p, and B are the coefficients for Auger recombination, direct recombination, and n_0 and p_0 are the intrinsic semiconductor electron and hole concentrations, respectively. $N(x,t)$ and $P(x,t)$ are functions of electron and hole concentrations with respect to position and time. t_0 and τ are the time at which the peak of the pump light occurs and the pulse's time width, respectively. The optical field generated by the pump light interference has only a component along the z-direction. Taking the SOI framework as the subject of study, the optical field reflects at the surface of the cladding-waveguide, resulting in energy loss, which is accounted for by the constant R. For commonly used pump light with a wavelength of 800 nm, the silicon material has an absorption depth of approximately 80 μm, which is much greater than the typical waveguide thickness of 220 nm to 340 nm. Additionally, compared to the x-direction, the intensity distribution in the y-direction changes slowly. Therefore, it is assumed that the intensity is sufficiently uniform in both the z and y directions, allowing for the neglect of carrier diffusion in these two dimensions. As mentioned earlier, only the periodic part of the optical intensity has the effect of a grating. Carrier diffusion in the x-direction significantly affects the duration of the periodic part. Therefore, considering the diffusion process, the above theoretical model is further modified as follows:

$$\frac{\partial N(x,t)}{\partial t} = \alpha(1-R)I(x,t)/h\nu + \beta(1-R)I(x,t)^2/2h\nu + D_n\frac{\partial^2 N(x,t)}{\partial x^2}$$

$$-C_n[N(x,t)^2 P(x,t) - n_0^2 p_0] - C_p[N(x,t)P(x,t)^2 - n_0 p_0^2] - B[N(x,t)P(x,t) - n_0 p_0] \tag{11}$$

$$\frac{\partial P(x,t)}{\partial t} = \alpha(1-R)I(x,t)/h\nu + \beta(1-R)I(x,t)^2/2h\nu + D_p\frac{\partial^2 P(x,t)}{\partial x^2}$$

$$-C_n[N(x,t)^2 P(x,t) - n_0^2 p_0] - C_p[N(x,t)P(x,t)^2 - n_0 p_0^2] - B[N(x,t)P(x,t) - n_0 p_0] \tag{12}$$

D_n and D_p are the bipolar diffusion coefficients for electrons and holes, respectively.

4.3 Numerical Calculation Results

This subsection discusses the numerical calculation results of above theoretical model with using The FTCS(Forward in Time, Central in Space) Explicit Method. Substituting the specific parameters listed in Table 1 allows for numerical calculations of the spatial distribution of carrier density evolving over time. The boundary condition are set as the gradient of carrier equals to zero at the boundary($x = \pm 30\mu m$). To ensure the convergence of the results, the stability condition $\delta t < \delta^2 x/2D_n$ is required.

In the scenario with a pulse width of 10 ps, the evolution of pump intensity distribution $I(x,t)$, electron concentration distribution $N(x,t)$, and hole concentration distribution $P(x,t)$ over time is depicted in Figure. 3(a), 4(b), and 4(c), respectively. The spatial periodic distribution of the pump light induces a similar spatial distribution of carriers. the range of the periodic part of $N(x,t)$ and $P(x,t)$ are illustrated as Δ_N and Δ_P in Figure.3 (d), due to carrier diffusion, they manifest a relative fast decay. Additionally, Δ_N exhibit a faster decay compared to holes, as shown in Figure. 3(d), which provides 9 time snapshots of the simulation process for both carriers from 10 ps to 90 ps. Considering the device should not be damaged, the magnitude of the pump light intensity in this simulation is about 2 orders of magnitude below the damage threshold($283.54W \cdot um^{-2}@10ps, 800nm$), and the Auger recombination effect is not prominent. The direct radiative recombination lifetime is much longer compared to the Δ decay process, so there is no significant change in the non-periodic part within the computed time range.

The process of Δ evolving over time is plotted in Figure. 4 for three different pump modes (10 ps, 10 ns, CW). The power for all three pump modes is set to be about one order of magnitude below the damage threshold. For the 10 ps pump pulse, the peak carrier concentration reaches approximately $10^{20}cm^{-3}$. Because the pump pulse width is much smaller than the time scale of diffusion, carrier generation occurs faster than diffusion, and both carrier peaks are close to each other and lag behind the pump peak in time. However, the lifetime of Δ_P is obviously longer than that of electrons. This lifetime can be roughly estimated as $\tau_{\Delta_P} \approx (\Lambda/2)^2/D_P \approx 53.25$ ps, which is comprehended as the time needed for a hole move from one peak of $P(x)$ to the nearest valley and it is as the same order of the numerically calculation. Compared to the lifetime of Δ_N. after the pump pulse ends, changes in refractive index are primarily caused by holes.

For the 10 ns pump pulse, the diffusion effect becomes prominent within the pump duration, and both carrier concentration peaks reach the order of $10^{18}cm^{-3}$ with nearly identical durations. Δ_N is one-third of that for holes, corresponding to the difference in their diffusion coefficients. In the case of CW pumping, Δ_N reaches equilibrium in about 100 ps, while Δ_P stabilizes in about 300 ps. The stabilized concentration for holes is approximately three times that of electrons, which corresponds to their respective diffusion coefficients. The peak values are on the order of $10^{15}cm^{-3}$.

In summary, using a shorter pump pulse width allows testing at higher pump intensity in experiments. In this case, the refractive index changes significantly, leading to higher diffraction efficiency. However, this state only lasts for about 50 ps. One testing method is to use a CW probe with sufficiently high time resolution detectors.

Alternatively, pulse-form probe can be used with coarse measurement time precision. By adjusting the delay between the local probe out of the chip and the diffracted signal within the autocorrelation optical path range, interference signals of both can be measured to obtain the diffraction signal intensity. The advantage of using continuous light as pump is that the grating remains present continuously. However, the induced refractive index change is too low, and the diffraction light intensity may be submerged in waveguide scattering or other noises. Specific feasible experimental methods are discussed in the sixth section. In the next section, the impact of pump peak intensity and grating radius on diffraction efficiency and far-field divergence angle will be analyzed using FDTD simulations for a 10 ps pulse width.

Coefficient	Physical Meaning	Value
α	SPA Coefficient @800nm	$8.5 \times 10^2 cm^{-1}$
β	TPA Coefficient @800nm	$1.0 \times 10^{-14} cm \cdot W^{-1}$
C_n	Auger Recombination Coefficient	$1.1 \times 10^{-30} cm^6 \cdot s^{-1}$
C_p	Auger Recombination Coefficient	$0.3 \times 10^{-30} cm^6 \cdot s^{-1}$
B	Radiative Recombination Coefficient	$1.1 \times 10^{-14} cm^{-3} \cdot s^{-1}$
n_0, p_0	Intrinsic Carrier Concentration Coefficient	$1.0 \times 10^{10} cm^{-3}$
D_n	Electrons Diffusion Coefficient	$5.0 cm^2 \cdot s^{-1}$
D_p	Holes Diffusion Coefficient	$1.7/3 cm^2 \cdot s^{-1}$

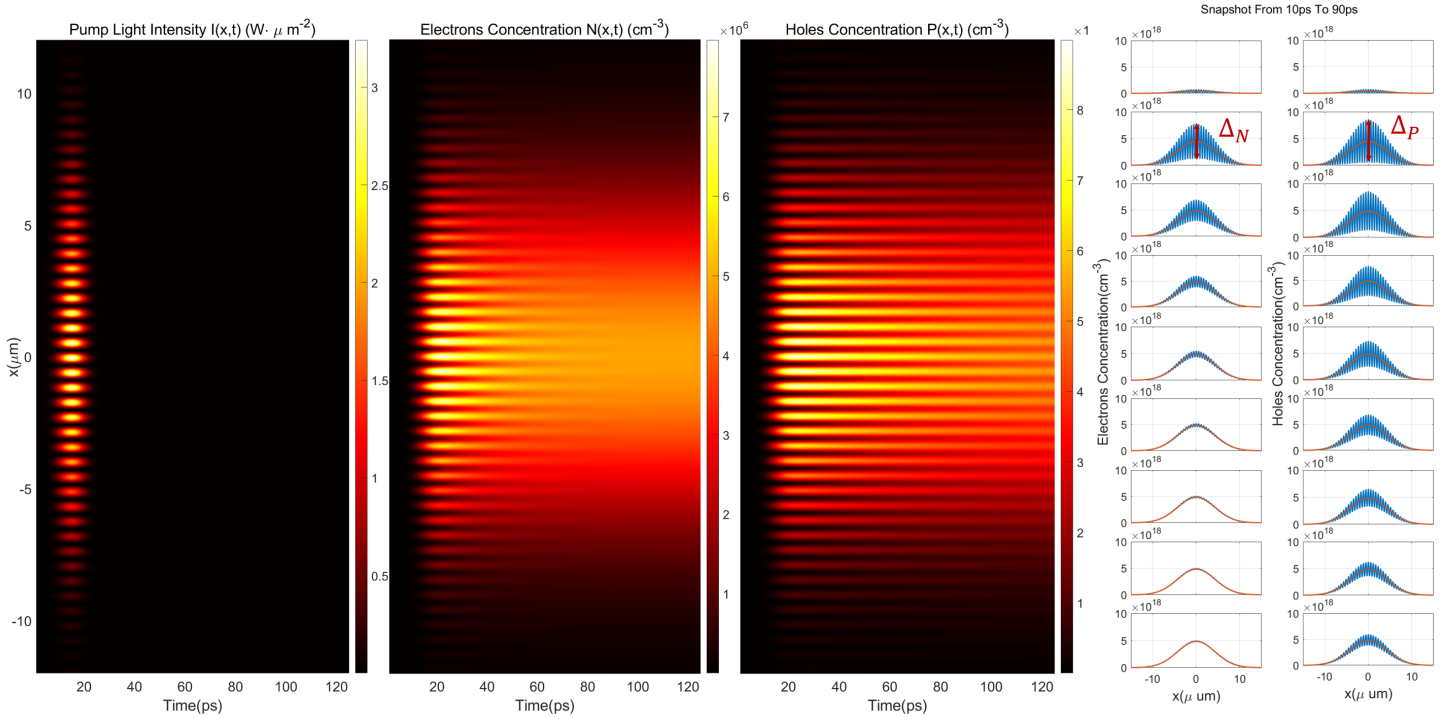**Table. 1** Numerical calculation parameters.

Figure. 3 (a) Evolution of the interfered optical field distribution at the waveguide surface over time: $I(x,t)$, with a pulse width set to 10 ps and I_0 set to $1 W \cdot um^{-2}$. **(b)**Evolution of the electron concentration distribution over time: $N(x,t)$. **(c)**Evolution of the hole concentration distribution over time: $P(x,t)$. **(d)**Time snapshots of the concentration distribution for both types of carriers from the calculated results in (b) and (c). The red line in the figures represents the move mean of $N(x,t)$ and $P(x,t)$. Δ_P and Δ_N are the range of periodic parts as illustrated,

which equals to the range of the origion signal minus the move mean signal.
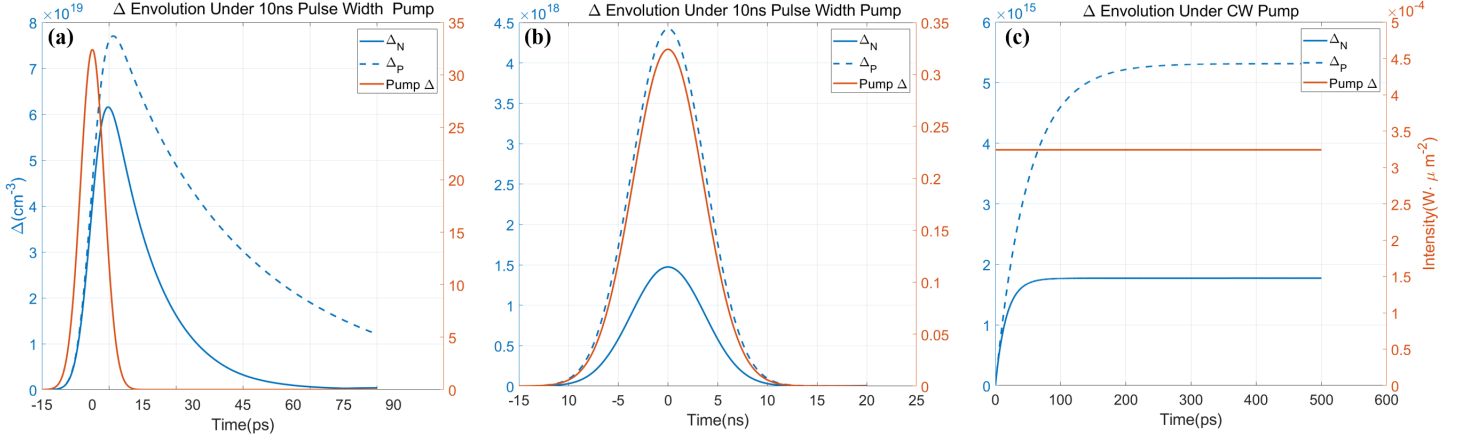

Figure. 4 (a) Evolution of the interfered optical field distribution, the periodic part's range of electron concentration and hole concentration spatial distribution Δ_N and Δ_P, for a pulse width of 10 ps with $I_0 = 10 W \cdot um^{-2}$. **(b)** Evolution of the interfered optical field distribution, the periodic part's range Δ electron concentration and hole concentration spatial distribution, for a pulse width of 10 ns with $I_0 = 0.1 W \cdot um^{-2}$. **(c)** Case of continuous-wave pump light, $I_0 = 0.0001 W \cdot um^{-2}$.

5 FDTD Simulation

5.1 Diffraction Efficiency

Diffraction efficiency is a crucial metric for assessing the capabilities of carrier gratings, and its quantitative calculation can be traced back to the diffraction formula for ultrasonic waves[22]. Ultrasonic waves excite periodic stress distributions within materials, thereby generating sinusoidal refractive index distributions. The first-order diffraction efficiency for this grating can be expressed as follows:

$$\eta = \frac{I_1}{I_0} = |J_1[\frac{2\pi d(\Delta n + i\Delta k)}{\lambda}]|^2 \tag{13}$$

Where I_0 and I_1 represent the intensities of the incident and first-order diffracted light, respectively, and d denotes the penetration depth of ultrasound in the material. J_1 is the first-order Bessel function. Subsequent literature also suggests[23,24] that, when the change in refractive index is small or the grating thickness is low, the Bessel function can be approximated as a quadratic function:

$$\eta \propto |\Delta n + i\Delta k|^2$$
$$\eta \approx (\frac{\pi\Delta nd}{\lambda})^2 + (\frac{\pi\Delta kd}{\lambda})^2 \tag{14}$$

In the context discussed in this paper, the aforementioned equations are not applicable. This is because, considering the influence of the grating dimensions, the number of stripes is not sufficient to approximate them as a sinusoidal grating. Furthermore, in the SOI system, incident light does not originate from free space and impinge directly onto the grating; rather, it passes through the waveguide structure before encountering the grating. Due to free carrier absorption, its intensity undergoes non-uniform attenuation along the propagation direction, influenced by the free carrier absorption. Therefore, providing a quantitative analysis of diffraction efficiency within the SOI framework is a complex mathematical process. Numerical calculations using the Finite-Difference Time-Domain (FDTD) method can offer a more efficient means of obtaining extensive data in this SOI context.

5.2 Simulation Settings

In light of the preceding analysis, the evolution of carrier concentration distributions $N(r,t)$ and $P(r,t)$ can be computed by equations (10)-(12). These distributions can be transformed into the refractive index distribution at each moment $\tilde{n}(r,t) = n(r,t) + ik(r,t)$ using empirical formulas (3). This distribution corresponds to a diffraction efficiency $\eta(t)$. The diffraction power $P(t)$ at a specific cross-section s can be calculated as $P(t) = \int_s I_0 \eta(t)ds$. For different moments in time when $\tilde{n}(r,t)$ varies, the diffraction efficiency η_{max} corresponding to the moment when the range of periodic part of $|\tilde{n}|$ is maximum, denoted as $\Delta|\tilde{n}|_{max}$, is the most significant. Calculating η_{max} allows for the most efficient analysis of the impact of various pump parameters settings.

The simulation section of this study considers a 60 μm long, 1 μm wide, and 220 nm thick SOI waveguide. A 1550 nm fundamental mode is chosen as the input at one end of the waveguide, as shown in Figure 5(a). In the y-direction, the grid resolution is 0.1 μm, while in the z-direction, it is 0.02 μm. Under this level of mesh precision, the effective refractive index of the propagating mode falls within the convergence range. The grid resolution in the x-direction has been adjusted to one-fifteenth of the grating period 0.5647 μm, approximately 0.0376 μm. This grating period's wave vector precisely results in diffraction signals with vertical emission. A single-beam pump light is incident on the silicon and silicon dioxide surfaces with a pulse width of 10 ps. The peak pump intensities I_0 are set to $1, 2, 4, 6, 8, 10, 20, 40, 60, 80, 100 W \cdot \mu m^{-2}$. To ensure a large sweep of parameters, the last set of pump peak intensity generates a interference intensity distribution whose maximum reaches damage threshold. Considering the choice of detection spatial resolution, for each intensity, the grating radius r_0 is taken as $1, 2, 4, 6, 8, 10 \mu m$. The refractive index distribution $\tilde{n}(r,t)$ corresponding to $\Delta|\tilde{n}|_{max}$ is obtained numerically by Matlab for different sets of parameters. The import(n,k) function in Lumerical's FDTD module is used to import this refractive index distribution. All refractive index distributions are set within a region centered at x $= 0$ μm and spanning $\pm 30 \mu m$.

5.3 Results and Discussions

Figure 5(b) illustrates the transmittance on the upper surface of the waveguide under the specified variable conditions. Due to the constant grating period, increasing the grating radius can enhance the number of stripes involved in diffraction. Therefore, it can be observed from the figure that under different light intensity conditions, there is a noticeable increase in transmittance when the pump light spot radius changes from 2 μm to 4 μm. However, when the radius changes from 4 μm to 10 μm, the increase in transmittance becomes less pronounced. In fact, at pump peak intensities exceeding $40W \cdot \mu m^{-2}$, increasing the radius beyond a certain threshold can lead to a reduction in transmittance. This is because the free carrier grating not only modulates the real part of the material's refractive index but also modulates the imaginary part of the refractive index. The absorption by free carriers reduces the energy of the probing light, resulting in decreased diffraction efficiency. With a comparision between power distribution of no grating configuration and $I_0 = 100W \cdot \mu m^{-2}$, $r_0 = 10 \mu m$ pump setting configuration, it can be suggested that the power loss is not as a result of scattering from index variations. This suggests that the impact of increasing the number of stripes on diffraction efficiency is nonlinear and gradually diminishes as the radius of the free carrier grating increases. Beyond a certain threshold, increasing the number of stripes cannot offset the negative effects of free carrier absorption. This effect becomes more significant at higher pump light intensities.
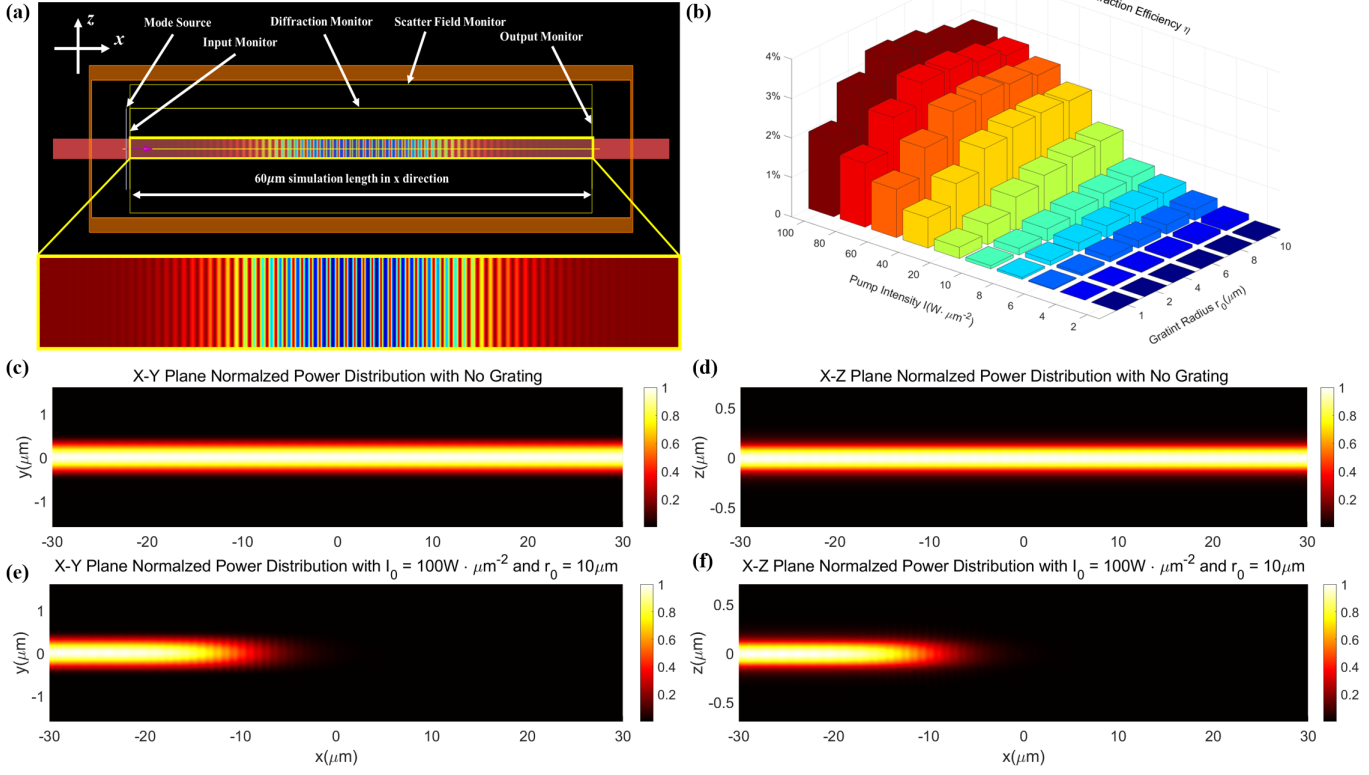
Figure. 5 (a) Illustration of FDTD simulation configuration, including necessary monitors and detailed nk map. **(b)**Diffraction transmittance with different pump sets, including pump peak intensity and grating radius. **(c)-(f)**Power Distribution in the X-Y plane and X-Z plane of no grating and $I_0 = 100W \cdot \mu m^{-2}, r_0 = 10\mu m$ pump setting.

Figure 6 displays the far-field analysis. Lumerical's far-field functionality enables the calculation of the superposition of the electromagnetic field on a spherical surface located 1 meter away from a specified monitor. Consequently, the far-field angular distribution on the upper surface of the waveguide can be computed. Figure 6(a) presents the normalized far-field distribution for a pump peak intensity of $4W \cdot \mu m^{-2}$ (i.e., the maximum values of the far-field intensity data for the six radius settings are scaled to 1). As the radius increases, the far-field distribution gradually becomes more concentrated, and the central intensity significantly increases. However, in the case depicted in Figure 6(b) near the damage threshold of $100W \cdot \mu m^{-2}$, the far-field center shifts by approximately $-18°$, and as the radius increases, sidelobes with increasing intensity appear on the right side of the main beam, severely affecting the concentration of the far-field beam.

Figure 6(c) illustrates the influence of different radii on the far-field center and far-field divergence angle under a specific pump peak intensity. The horizontal axis of the rectangle represents the center of the optical field, the vertical axis represents the corresponding radius of the free carrier grating, and the length of the rectangle represents the half-angle width of the far-field, with each black line displaying the vertical direction. As the pump intensity increases, the far-field angle gradually shifts away from the center. When the intensity reaches $80W \cdot \mu m^{-2}$, increasing the radius leads to sidelobes and worsens the half-angle width. This implies that increasing both the intensity and the radius not only fails to enhance diffraction efficiency but also reduces the concentration of the far-field beam, which has a detrimental effect on practical measurements.

Above results can be explained as following analysis. As mentioned in section 3, the phase matching condition:

$$\frac{2\pi n_{eff}}{\lambda_{probe}} - \frac{2\pi}{\Lambda} = \frac{2\pi n_{cladding}}{\lambda_{probe}} sin(\theta) \tag{15}$$

11

Under the configuration of vertically emission, above equation's LHS should equal to 0. However, this pre-assumes n_{eff} is a constant. In fact, carrier induced FCI effect reduces the real part of refractive index, rendering n_{eff} decrease. Therefore, LHS is less than 0, which induces a negative of θ in RHS of the equation. To eliminate the shift from vertical emission, one should increase Λ. Cosidering θ equals to $-18°$, $\Lambda' = [n_{eff} - n_{cladding}sin(\theta)]/\lambda_{probe} \approx 0.6751\mu m$, which is 20% greater than the origin one. And the pumping angle ϕ reduces from $45°$ to about $36°$. More over, at a certain pump intensity, the radius increasing also leads to a slightly shift of the center direction at far-field. This is becasue higher grating radius causes a larger region of low refractive index region, effectively reduce the n_{eff} of the mode.

The sidelobes caused by higher pump intensity are the result of truncated Gaussian envelop of the near field. Far-field distribution can be treated as the Fourier Transform of the near field distribution. In lower pump intensity, the field of the waveguide's unpper surface is a periodical field modulated by a entire Gaussian-shaped envelop, leading to a large main angle at far-field. However, the FCA effect induced by hign pump intensity reduced mode intensity along the x direction, truncating the field's Gaussion envelop with a fast decaly at the right side of the envelop's center, causing an unsymmetric near field which leads to sidelobes at far-field.
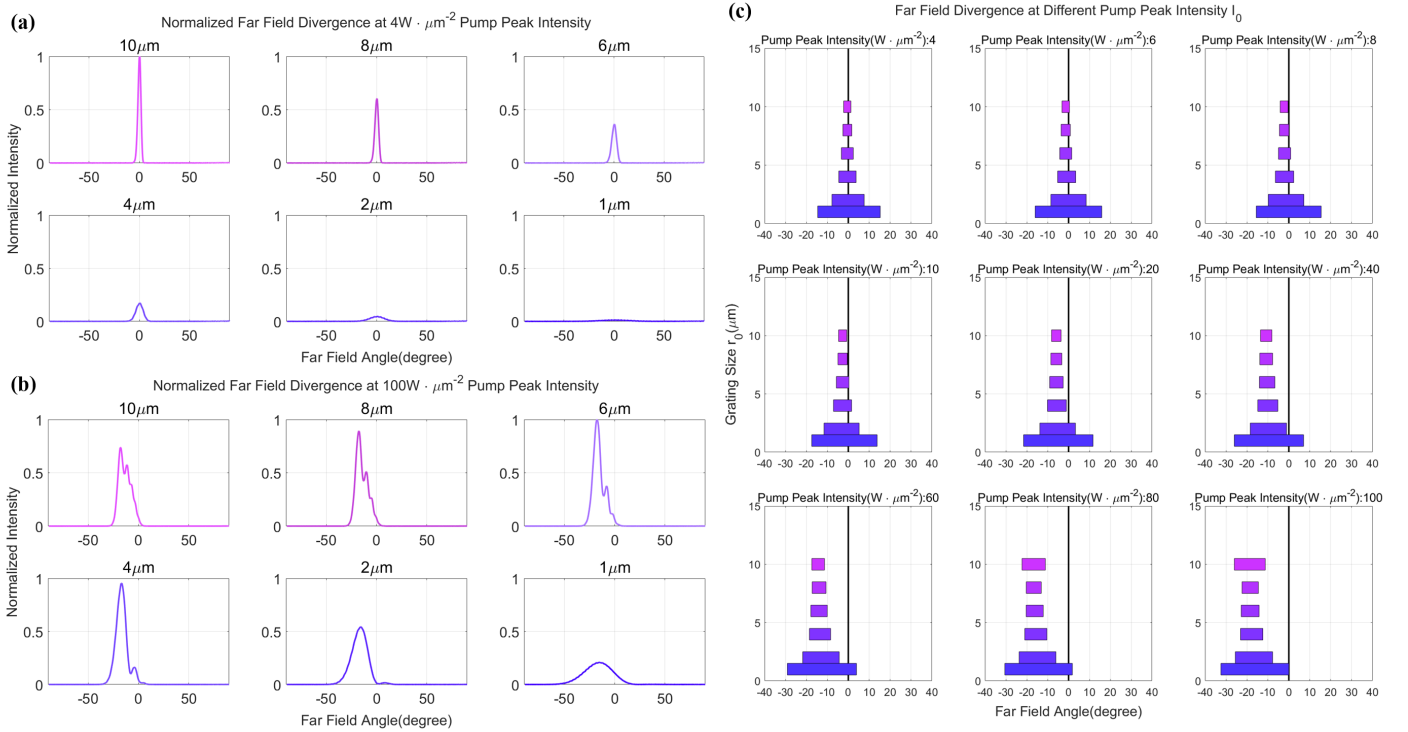

Figure. 6 (a) Illustration of carrier grating far-field angular distribution under the pump with peak intensity $I_0 = 4W \cdot \mu m^{-2}$. **(b)**Illustration of carrier grating farfield angular distributionunder the pump with peak intensity of $I_0 = 100W \cdot \mu m^{-2}$. **(c)**Illustration of half-widh and direction of central peaks of the far-field of different pump sets.

6 Experiment Feasibility

Based on the theoretical analysis of carrier dynamics and FDTD simulations of refractive index distribution presented in above sections, we can now discuss the feasibility of various experimental approaches.

6.1 Choice of Pump

Firstly, let's consider the choice of laser source:

12

1. Nanosecond Pulse Laser or CW laser: Using nanosecond or continuous-wave lasers may result in pump peak intensities that are too low. The maximum of refractive index change induced by nanosecond or continuous-wave pumping is less than 10^{-2}, leading to diffraction efficiencies lower than -40 dB for the waveguide mode. This makes it difficult to distinguish diffraction signals from scattered light introduced by waveguide surface roughness. However, using continuous-wave light with ultra small bandwidth for pump in the SOI system maybe feasible if the pump is modulated. Lock-in amplification of the diffraction signal may help to separate it from the scattered signal. This configuration is shown as Figure. 7(a).

2. Picosecond Pulse Laser: Picosecond lasers can achieve diffraction efficiencies exceeding -20 dB. By appropriately increasing the radius of the free carrier grating and the pump intensity, diffraction efficiency can be optimized. However, as discussed earlier, there are limitations when the pump peak intensity on the waveguide surface exceeds $40W \cdot \mu m^{-2}$. One concern is the detrimental effect of increased free carrier absorption on diffraction efficiency, while the other is the adverse impact of sidelobes on the concentration of the far-field beam, affecting the measurement of diffraction signals.

2.a. As shown in Figure. 7(b), If continuous-wave light is chosen as the probe, higher temporal precision is required for the diffraction light detector. In this case, the presence of the pulse laser is very short-lived, and the time window for the appearance of the diffraction signal is on the picosecond timescale. A time resolution smaller than this timescale is needed for accurate measurements.

2.b. As shown in Figure. 7(c), If pulsed light is chosen for probing, a delay setup is required to interfere the diffraction signal with a local probe signal using autocorrelation methods. The advantage of this approach is that the time resolution requirements for measurements can be reduced.

2.c. If a smaller pump radius is used or if the intensity is high, it can lead to an increase in the half-width of the far-field main peak of the diffraction signal. This may result in the expansion of the spatial distribution of intensity, necessitating refocusing of the diffraction signal. Otherwise, the reduced power per unit area can pose challenges for detection. If near-field diffraction signal reception is chosen, such as at the cladding surface, in this scenario, the divergence area of the diffraction light is smaller, which is more favorable for signal detection.

6.2 Control of Period Control

Another important consideration in the experiment is the control of the carrier grating period. For the mode of interest (e.g., TE mode, TM mode, or higher-order modes), the required grating period can be calculated through phase matching.

1. If the waveguide has a cladding, to prevent power loss due to oblique incidence at the interface and the appearance of higher-order diffraction signals, the emission direction can be chosen to be perpendicular to the upper surface of the waveguide. According to the FDTD simulation results, increasing the pump intensity can alter the emission direction. Experimenters need to adjust the pumping angle based on specific simulation results to ensure that the center of the far-field optical field is in the vertical direction.

2.If there is no cladding, further calculations are needed to determine the optimal emission angle. This is because as the diffraction direction becomes smaller relative to the mode propagation direction, the required grating period increases. Carriers need more time to move from one peak to the nearest valley in the periodic distribution, resulting in a longer presence of the grating, which increases the total diffraction energy. However, smaller angles introduce more diffraction signal orders, which reduces the signal strength of the main order. The combined effects require experimenters to simulate and determine using the methods discussed in this paper before conducting the experiment.

6.3 Control of Carrier Grating Radius

Since high spatial resolution approach requires interference between two pump beams in a spatial range on the order of 10 μm, careful consideration is needed when adjusting the carrier grating's radius. Commonly used spatial optical modules have apertures that are too large compared to the working distance, limiting the possibility of focusing and interfering two beams of light in such a confined space. The use of two fiber lenses can achieve the desired outcome (as shown in Figure 8(d)). The Gaussian beam waist radius w_0 output by the conical fiber lens is on the order of micrometers and can be controlled by adjusting the angle ψ and curvature r_f of the top cone to control the beam waist radius w_0 and distance z_0. If it is necessary to increase the optical intensity in the waveguide width direction, one can also choose a wedge-shaped fiber to output an elliptical beam, thereby reducing the beam radius in the y-direction and increasing the pump power density. Moreover, using lensed fibers for near-field collection of the detection light is also a feasible approach to consider. Additionally, if the spatial resolution of the spatial light modulator is sufficiently small compared to the grating period, it can also be a viable option.
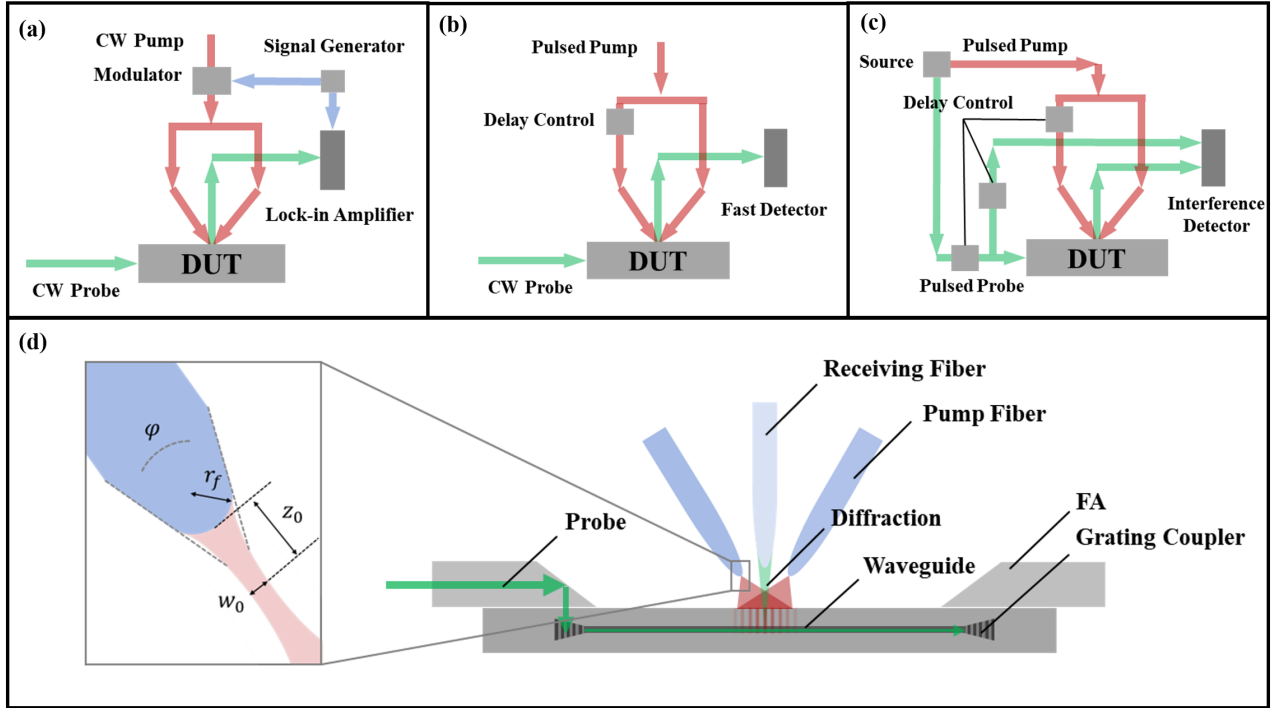

Figure. 7 **(a)**Configuration with using CW form of pump. **(b)**Configuration with using Pulsed form of pump and CW form of probe. **(c)**Configuration with using Pulsed form of pump and Pulsed form of probe. **(d)**Illustration of a feasible experiment design with using lensed fibers as pumping and receiving. The probe signal is injected into the chip by Fiber Arrays and Grating coupler, passing through the Device Under Test(DUT) and diffracting out by the carrier grating which is generated by the pump. The diffraction signal is received by a conical lensed fiber placed at specific location. The pump is guided by two lens fibers alligned with pre-desiged angle.

6.4 Conclusion and Improvements

Although the theoretical and simulation framework is based on the SOI system, the concept can be extended to other similar on-chip systems. Firstly, it is necessary to determine the semiconductor characteristics of the material used in the system detected. This includes parameters such as bandgap width, optical absorption characteristics, carrier generation, recombination, diffusion properties, as well as FCI and FCA parameters. Secondly, establish the damage threshold of the material to avoid damaging the chip due to excessively high laser power. Thirdly,

identify the modes of interest for detection and perform grating period analysis. This technique involves numerical calculations based on partial differential equations and FDTD simulations to determine the pump intensity and carrier grating radius. These parameters are critical for optimizing diffraction efficiency, far-field beam divergence angle, with a need of high detection spatial resolution.

There are several directions for further refinement and investigation in this work: 1. Consideration of Edge Recombination: The influence of edge recombination has not been accounted for in both theory and simulations. For narrow waveguides, the distribution and diffusion of carriers in the y-direction need to be incorporated into the computational framework.

2. Wavelength Dependence: The pump wavelength has been considered as a single value. However, the skin depth, and carrier generation characteristics for other pump wavelengths may lead to non-uniform carrier diffusion behavior along the waveguide thickness direction.

3. Non-Uniform Carrier Diffusion: The non-uniformity in electron and hole diffusion could introduce variations in electric field distribution, which in turn can cause more complex carrier diffusion behavior.

4. Impact of Grating Period on Δ_N, Δ_P Lifetime: The effect of the grating period on Δ_N, Δ_P lifetime has not been considered in numerical calculations. Additionally, FDTD simulations have not accounted for diffraction efficiency and far-field divergence characteristics under non-vertical emission conditions.

These areas warrant further investigation to enhance the comprehensiveness of the study and to gain a deeper understanding of the behavior of carrier gratings in integrated photonics systems.

7   Conclusion

This work provides a brief overview of the fundamental principles of TGS technology and its previous applications in silicon bulk materials and on-chip SOI systems. It proposes an integrated photonics chip detection scheme based on carrier grating and briefly analyzes the grating wavevectors, plasmonic effects, and damage thresholds in SOI strip waveguides. A carrier dynamics model is established, and numerical calculations are performed to assess the impact of different pump pulse widths on carrier recombination and diffusion in the SOI configuration within the range of damage threshold limitations. Leveraging the plasmonic effects based on carrier distribution, this work introduces refractive index distributions into FDTD simulations to compute carrier grating diffraction efficiency and far-field divergence characteristics under various parameter settings. The results indicate that above $4\mu m$, the higher pump peak intensity induces negative effects on diffraction efficiency and far-field concentration as grating radius increases. Finally, the feasibility of the experimental approach is discussed, along with specific directions for potential improvements in both theory and simulation.

8   Appendix

9   Reference